Nitrogen Fixation | Hot Paper |

Bio-Inspired Aerobic-Hydrophobic Janus Interface on Partially Carbonized Iron Heterostructure Promotes Bifunctional Nitrogen Fixation

Wei Zong,+ Haiqi Gao,+ Yue Ouyang,+ Kaibin Chu, Hele Guo, Leiqian Zhang, Wei Zhang, Ruwei Chen, Yuhang Dai, Fei Guo, Jiexin Zhu, Zhenfang Zhang, Chumei Ye, Yue-E. Miao,* Johan Hofkens, Feili Lai,* and Tianxi Liu*

Abstract: Competition from hydrogen/oxygen evolution reactions and low solubility of N_2 in aqueous systems limited the selectivity and activity on nitrogen fixation reaction. Herein, we design an aerobic-hydrophobic Janus structure by introducing fluorinated modification on porous carbon nanofibers embedded with partially carbonized iron heterojunctions (Fe₃C/Fe@PCNF-F). The simulations prove that the Janus structure can keep the internal Fe₃C/Fe@PCNF-F away from water infiltration and endow a N_2 molecular-concentrating effect, suppressing the competing reactions and overcoming the mass-transfer limitations to build a robust "quasi-solid–gas" state micro-domain around the catalyst surface. In this proof-of-concept system, the Fe₃C/Fe@PCNF-F exhibits excellent electrocatalytic performance for nitrogen fixation (NH₃ yield rate up to 29.2 $\mu g\,h^{-1}\,mg^{-1}_{cat.}$ and Faraday efficiency (FE) up to 27.8 % in nitrogen reduction reaction; NO₃⁻ yield rate up to 15.7 $\mu g\,h^{-1}\,mg^{-1}_{cat.}$ and FE up to 3.4 % in nitrogen oxidation reaction).

Introduction

Nitrogen chemistry is essential for the sustainability of all life forms and the development of numerous industrial processes.[1–3] In nature, an important pathway for nitrogen fixation is through a class of enzymes known as nitrogenases, which have, however, a low efficiency. This, together with increasing demands in agriculture, has given rise to booming synthetic nitrogen industries: (1) The nitrate industry relies on the Ostwald process by multi-step NH₃ oxidation reactions under harsh conditions (i.e., 673–873 K, 15–25 MPa);[4–7] (2) The ammonia industry is highly supported by the famous Haber-Bosch process to reduce N_2 with H_2 molecules at high pressure (20–30 MPa) and temperature (over 773 K).[8–10] Therefore, both the Ostwald and Haber-Bosch processes are energy-intensive (1–2 % of global energy consumption) and subsequently responsible for massive carbon dioxide emissions ($\approx$ 420 Mt per year). As a result, there is an urgent need to explore energy-efficient and environmentally sustainable alternative techniques for artificial N_2 fixation. Among various (bio)chemical strategies, electrochemical nitrogen oxidation reaction (NOR)

[*] W. Zong,+ K. Chu, L. Zhang, Prof. T. Liu
Key Laboratory of Synthetic and Biological Colloids, Ministry of Education, School of Chemical and Material Engineering, International Joint Research Laboratory for Nano Energy Composites, Jiangnan University
Wuxi 214122 (P. R. China)
E-mail: txliu@jiangnan.edu.cn

H. Gao+
State Key Laboratory of Organic Electronics and Information Displays&Institute of Advanced Materials (IAM), Nanjing University of Posts&Telecommunications
Nanjing 210023 (P. R. China)

W. Zong,+ Y. Ouyang,+ Dr. Y.-E. Miao, Prof. T. Liu
State Key Laboratory for Modification of Chemical Fibers and Polymer Materials, College of Materials Science and Engineering, Donghua University
Shanghai 201620 (P. R. China)
E-mail: yuee_miao@dhu.edu.cn

K. Chu, H. Guo, Prof. J. Hofkens, Dr. F. Lai
Department of Chemistry, KU Leuven
Celestijnenlaan 200F, 3001 Leuven (Belgium)
E-mail: feili.lai@kuleuven.be

W. Zong,+ W. Zhang, R. Chen, Y. Dai, F. Guo, J. Zhu, Z. Zhang
Christopher Ingold Laboratory, Department of Chemistry, University College London
20 Gordon Street, London WC1H 0AJ (UK)

C. Ye
Department of Materials Science and Metallurgy, University of Cambridge
Cambridge CB3 0FS (UK)

Prof. J. Hofkens, Dr. F. Lai
Department of Molecular Spectroscopy, Max Planck Institute for Polymer Research
Ackermannweg 10, 55128 Mainz (Germany)

[+] These authors contributed equally to this work.

and nitrogen reduction reaction (NRR) are promising technologies for nitrogen fixation under ambient conditions, which are powered by renewable electricity with inexhaustible water as the hydrogen/oxygen source instead of fossil fuels.[11–19] However, the current electrocatalysts can only achieve either NRR or NOR processes, which originates from the different reaction mechanisms between N_2–H_2O and N_2–O_2 coupling processes, making it urgent to construct advanced bi-functional electrocatalysts with reasonable structures and designs.

Iron, as one of the most abundant metals on earth, occurs in biological nitrogenases for natural N_2 fixation and therefore we reasoned that it is a promising candidate for bi-functional electrocatalysts of NRR and NOR processes.[20,21] However, the development of NRR and NOR electrocatalysts (not only for iron-based ones) is hampered by two challenges of low ammonia/nitrate yield rate and limited Faradaic efficiency. The low ammonia/nitrate yield rate originates from the high bond energy of the N≡N triple bond in chemically inert N_2 gas ($940.95 \text{ kJ mol}^{-1}$), resulting in sluggish adsorption and activation of N_2 molecule on the surface of electrocatalyst.[22–25] Recently, various strategies, including incorporating defect structures and heterojunction, have been put forward to regulate the charge distribution on the surface of the electrocatalyst and modulate the coupling behavior between the electrocatalyst and the N_2 molecule.[26–28] Attributing to the continuous charge redistribution around the two-phase boundary in the heterojunction, it can accept lone-pair electrons from N_2 and return electrons to the π orbitals of N_2, thus facilitating strong absorption and activation of N_2 to kinetically drive nitrogen fixation reaction. However, due to the low solubility of N_2 gas in aqueous-based electrolytes, the effective collision between N_2 molecule and electrocatalyst is confined dramatically. The well-designed active sites by the above-mentioned strategies would be fully occupied by abundant water molecules, leading to the overwhelming competing water splitting reactions, including hydrogen evolution reaction (HER) and oxygen evolution reaction (OER), and limited Faradaic efficiency for nitrogen fixations (NRR and NOR).[29,30] In order to improve the nitrogen fixation performance efficiently and selectively, the modulation of the mass transfer near the catalyst interface can be a feasible strategy to surmount the above challenges.[31] It has been proven as a useful method to limit H_2O accessibility by constructing a hydrophobic layer between the electrolyte and the electrocatalyst, thereby inhibiting the H_2O-involved competing reactions.[32–37] However, the N_2 concentration around the catalyst in these methods is still low and locally uneven due to the uncontrollable and inhomogeneous coverage of hydrophobic layers, hindering the effective interaction of the solid catalyst with the gas, which makes it a pending challenge on how to suppress water electrolysis efficiently without any sacrifice of ammonia/nitrate yield rate.

Inspired by nature,[38,39] we introduced hydrophobicity based on the "abdomens villus effect" encountered in aquatic arachnids, such as the water spider (Argyroneta aquatica) in Figure 1a. The Argyroneta aquatica can capture air and breathe underwater owing to the hydrophobic villus on its abdomen. Hydrophobicity contributes to the trapping of gases when it is engineered in a micro-/nano-scale interfacial structure.[40,41] Herein, we report a selective and efficient bifunctional electrocatalyst for nitrogen fixation by constructing an aerobic-hydrophobic Janus structure, which is fluorinated porous carbon nanofibers embedded with partially carbonized iron heterojunctions (Fe$_3$C/Fe@PCNF-F). The aerobic-hydrophobic 1H, 1H, 2H, 2H-perfluorodecanethiol (pFDe) layer can keep the internal Fe$_3$C/Fe@PCNF-F away from water penetration and contribute to the diffusion N_2 gas that can be stored in the porous carbon nanofibers, resulting in local high N_2 concentrations. Therefore, the aerobic-hydrophobic Janus structure forms a robust "quasi-solid–gas"-state microenvironment around the catalyst for efficient nitrogen reduction and oxidation reactions (Figure 1a). Molecular dynamics (MD) and *COMSOL* Multiphysics simulations confirm the positive role of the Janus structure in preventing water infiltration and overcoming the overall limitations of gas mass transfer. Consequently, the Fe$_3$C/Fe@PCNF-F exhibits excellent electrocatalytic performance for nitrogen fixation (NH_3 yield rate up to $29.2 \text{ μg h}^{-1} \text{ mg}^{-1}_{\text{cat.}}$ and Faraday efficiency (FE) up to 27.8% in NRR; NO_3^- yield rate up to $15.7 \text{ μg h}^{-1} \text{ mg}^{-1}_{\text{cat.}}$ and FE up to 3.4% in NOR). Density functional theory calculations elucidate the catalytic reaction mechanism on the partially carbonized iron heterostructure and suggest reduced energy barriers, which can also be demonstrated from the in situ vibrational and mass spectrometry characterization with the successful detection of reaction intermediates experimentally to validate the nitrogen fixation reaction pathway.

Results and Discussion

To understand the function of the 1H, 1H, 2H, 2H-perfluorodecanethiol (pFDe) layer in constructing an aerobic-hydrophobic Janus interface, the nitrogen and water diffusions within pFDe (Figure S1) and blank models were carried out by molecular dynamics (MD) simulations, where a $0.1 \text{ M Na}_2\text{SO}_4$ solution supersaturated with nitrogen molecules was applied as the electrolyte. The initial configurations in the simulation boxes were set up by placing the water and nitrogen molecules at the top and bottom positions randomly, where the direction from top to bottom in the constructed model is defined as the Z-direction. The two-layer pFDe membranes stacked with pFDe molecules divide the simulation box into three parts along the Z-direction, while the counterpart is the blank box. Figures 1b and 1c show several snapshots for the distributions of N_2 and H_2O molecules in pFDe and blank models as function of diffusion times. When the diffusion time increases from 0 to 1000 ps, the N_2 molecules will gradually penetrate and stay between two pFDe layers, while most H_2O molecules are isolated outside the pFDe layer and unable to access the central part. In great contrast to the blank model, the H_2O molecules can spread freely in the simulation box to achieve a homogeneous distribution of H_2O molecules within a short
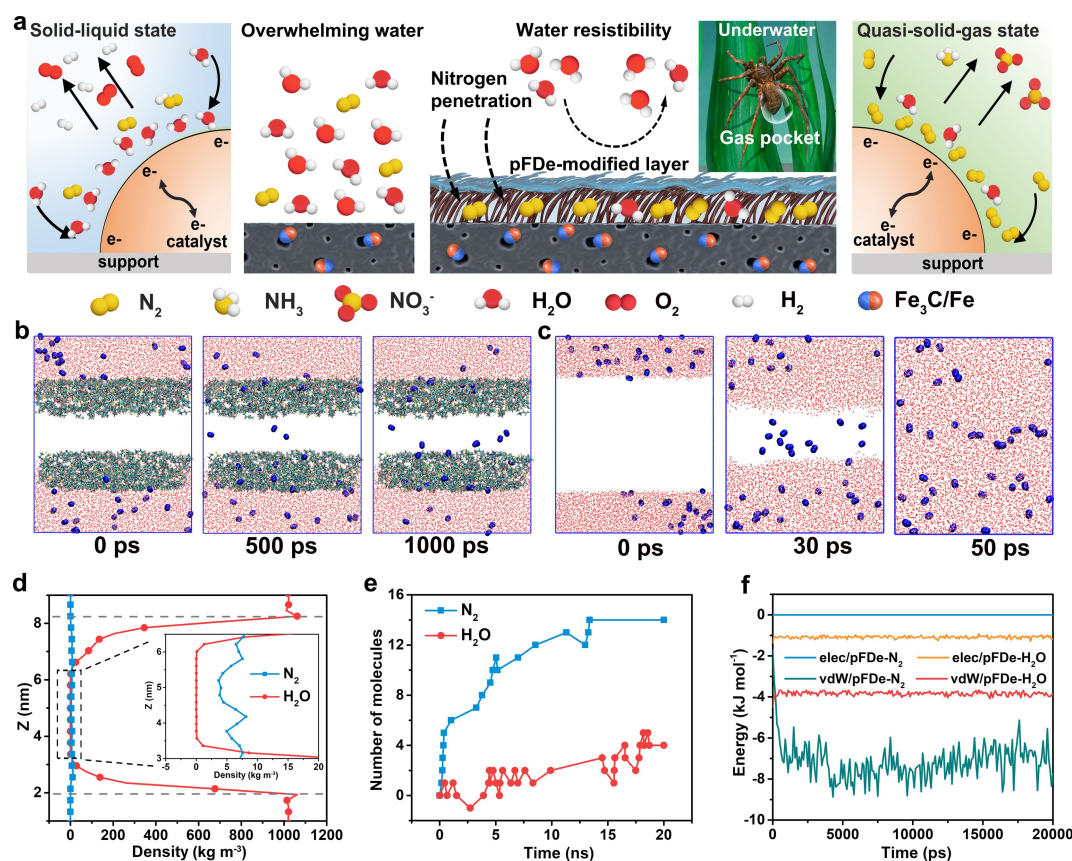
Figure 1. Introduction to the aerobic-hydrophobic Janus interface and MD simulations of N_2 and H_2O diffusion. a) Mechanism for improving the selectivity and activity of electrochemical nitrogen fixations (NRR and NOR processes) with/without an aerobic-hydrophobic Janus interface. Snapshots for the distributions of N_2 and H_2O molecules in b) pFDe model and c) blank model. Here, the cyan, yellow, red, white, and blue balls represent C, S, O, H, and N atoms, respectively. d) The average densities for N_2 and H_2O molecules along the Z-direction of pFDe model (from top to bottom in the simulation box). e) The number of N_2 and H_2O molecules within the pFDe layer from 0 to 20 ns. f) Electrostatic and vdW interactions of N_2 and H_2O molecules with pFDe molecules.

diffusion time of 50 ps (Figure S2). By taking the diffusion process from 9 to 10 ns as an example, the average density of H_2O molecules through positions of the pFDe layer (from 2.0 to 8.2 nm along the Z direction) drops dramatically (Figure 1d). After counting the N_2 and H_2O molecules that passed through the pFDe layers statistically, the N_2 molecules show a higher diffusion capacity than H_2O molecules (Figure 1e), indicating that the hydrophobic modification can inhibit the water penetration without affecting the nitrogen diffusion. Moreover, the investigations of the electrostatic and van der Waals (vdW) interactions between pFDe and N_2/H_2O molecules indicate that the coated pFDe layers show stronger vdW attractions towards N_2 molecules as compared to H_2O molecules (Figure 1f) and lead to the superior nitrogen adsorption capacities. These results confirm that the hydrophobic behavior of pFDe layer is beneficial to realizing a "quasi-gas-solid" state in the interior space as a localized high-concentration nitrogen region to favor the nitrogen fixation reactions (NRR and NOR) and suppressing the competing reactions (HER and OER).

Inspired by the concept revealed by MD simulations, we select partially carbonized iron heterostructure nanoparticles as the electrocatalyst to construct fluorinated porous

carbon nanofiber with aerobic-hydrophobic Janus interface by using sol-gel electrospinning, pyrolysis, and fluorinated modification (Figure S3). Initially, we prepared a stable sol by combining polyacrylonitrile (PAN), polyvinyl pyrrolidone (PVP), and various metal salts of iron(III) and zinc(II) acetates. The strong coordination between the metal ions and the carbonyl groups of the PVP molecules enabled the formation of PAN/PVP·Fe/Zn cross-linking networks, which contributed to the stability of the sol. Subsequently, the PAN/PVP·Fe/Zn sol was stretched rapidly by electrospinning technique to generate pliable gel-state Fe/Zn@PAN/PVP nanofiber films (Figure S4). After undergoing heterogeneous nucleation during the pyrolysis process, the uniformly dispersed iron ions within the metal-polymer nanofibers were changed into tiny iron oxide nanocrystals. As the gradual decomposition of PVP molecules under high temperature, abundant small organic molecules, such as hydrocarbons or CO, are produced to reduce the iron oxide nanoparticles (NPs) into Fe with partially carbonized Fe_3C heterostructure, namely $Fe_3C/Fe@PCNF$ (more details are discussed in Figure S5). Finally, the $Fe_3C/Fe@PCNF$ was modified with pFDe molecule to construct an aerobic-hydrophobic structure on the $Fe_3C/Fe@PCNF-F$. Field-

emission scanning electron microscopy (FESEM) image shows that the Fe₃C/Fe@PCNF-F nanofibers exhibit well-maintained fibrous morphology with an average diameter of about 250 nm (Figure S6), demonstrating that the metal-polymer interactions and the internal stress caused by pyrolysis allow for the localized nucleation and confined growth of Fe₃C/Fe NPs. The transmission electron microscopy (TEM) images (Figure 2a&S7) prove that Fe₃C/Fe NPs are confined in the nanofibers uniformly with ultrasmall sizes (≈15.3±2.1 nm in diameter). This result suggests that the strategy followed for preparing PAN/PVP·Fe/Zn sol is beneficial to not only in situ decomposing and transforming into ultrafine Fe₃C/Fe NPs but also avoiding aggregation of Fe NPs (Figure S8). The high-resolution TEM image (HR-TEM) presents distinct lattice fringes with interlayer spacings of 0.202 and 0.238 nm assigned to the (110) crystal plane of Fe and (121) crystal plane of Fe₃C, respectively (Figure 2b). The twinborn facets of Fe and Fe₃C crystals confirm the successful formation of partially carbonized Fe₃C/Fe heterostructure in the Fe₃C/Fe@PCNF-F. Energy-dispersive X-ray spectroscopy (EDS) elemental mappings (Figure 2c&S9) further certify the elemental composition of Fe₃C/Fe@PCNF-F with uniform distributions of C, O, Fe,

and F elements. The X-ray diffraction (XRD) pattern of Fe₃C/Fe@PCNF-F presented in Figure 2d shows an intense peak located at 26° corresponding to the (002) plane of graphite carbon and indicates its high graphitization degree. Meanwhile, the diffraction peaks located at 37.7°, 44.9°, 48.6°, 49.1°, and 44.6° can be well indexed to the (121), (031), (131), and (221) planes for Fe₃C and (110) plane for Fe, respectively. It is in good agreement with the HR-TEM results and demonstrates the co-existence of Fe₃C and Fe phases in Fe₃C/Fe@PCNF-F.[42]

The chemical state and coordination environment of the Fe₃C/Fe@PCNF-F were further investigated by X-ray photoelectron spectroscopy (XPS) and X-ray absorption spectroscopy (XAS) measurements. Apart from the observation of C 1s, O 1s, and Fe 2p in the XPS survey spectra, the existence of additional F 1s and S 1s peaks indicates the successful coating of pFDe layer on the surface of Fe₃C/Fe@PCNF-F (Figure S10). As shown in the high-resolution XPS Fe 2p spectrum of Fe₃C/Fe@PCNF-F (Figure 2e), two pairs of peaks at the binding energy of 707.2/719.7 eV and 708.5/720.9 eV can be attributed to Fe–Fe and Fe–C bonds, respectively, confirming the formation of partially carbonized Fe₃C phase in the metallic Fe matrix.[43] The specific
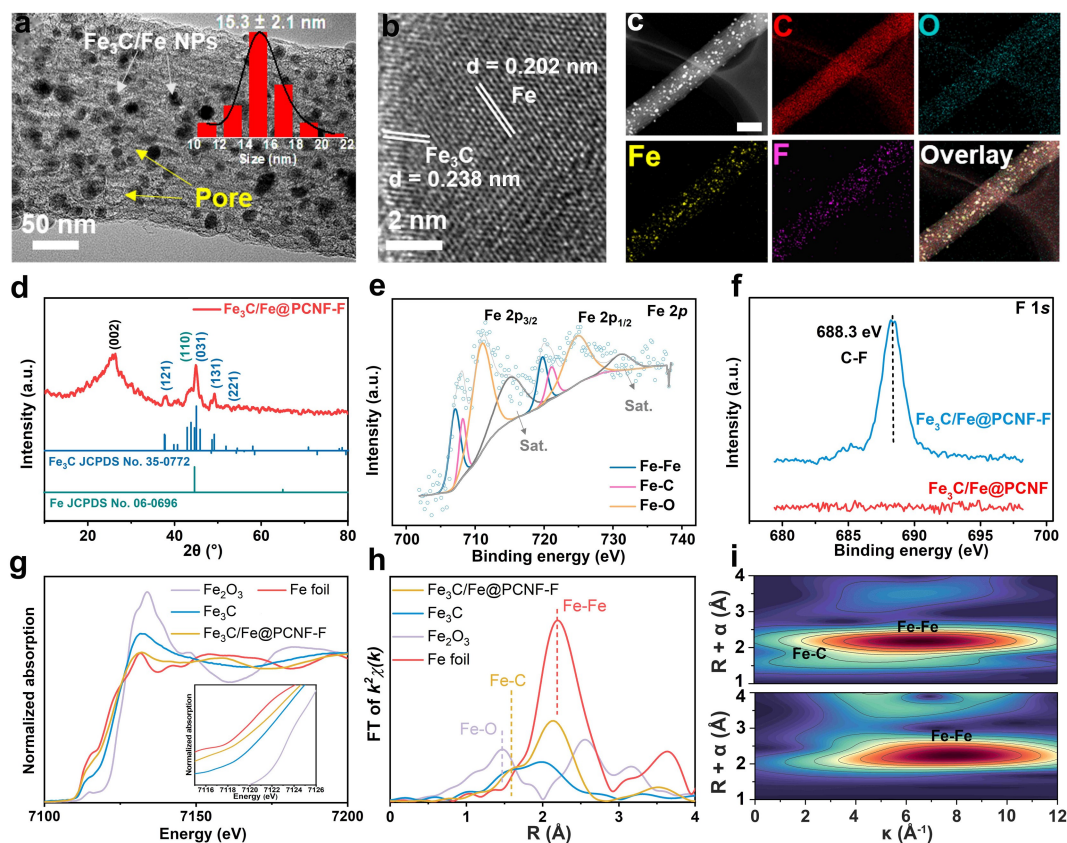

Figure 2. Structural characterization of Fe₃C/Fe@PCNF-F. a) TEM image of Fe₃C/Fe@PCNF-F (inset: particle size distribution of Fe₃C/Fe NPs). b) HR-TEM image of Fe₃C/Fe NPs. c) High-angle annular dark-field scanning TEM image and the corresponding element mappings for C, O, Fe, and F elements of Fe₃C/Fe@PCNF-F (Scale bar: 200 nm). d) XRD pattern of Fe₃C/Fe@PCNF-F. e) High-resolution XPS Fe 2p spectrum of Fe₃C/Fe@PCNF-F, and f) F 1s spectra of Fe₃C/Fe@PCNF and Fe₃C/Fe@PCNF-F. g) XANES spectra, h) FT-EXAFS spectra of Fe₃C/Fe@PCNF-F, Fe foil, Fe₃C, and Fe₂O₃. i) WT-EXAFS at K-edge of Fe₃C/Fe@PCNF-F and Fe foil.

ratio between Fe_3C and Fe can be determined by the corresponding peak areas, where the ratio of Fe to Fe_3C in $Fe_3C/Fe@PCNF-F$ is about 1.77:1.[44] Additionally, the F 1s spectrum of $Fe_3C/Fe@PCNF-F$ (Figure 2f) shows a distinct peak at 688.3 eV that can be attributed to the C–F bonds in the successfully coated pFDe layers. A series of Fe K-edge synchrotron radiation-based X-ray absorption near-edge structure (XANES) spectra were performed with Fe foil, Fe_3C, and Fe_2O_3 as the comparisons (Figure 2g). The Fe K-edge XANES spectrum of $Fe_3C/Fe@PCNF-F$ is positioned between the Fe foil and the Fe_3C (inset in Figure 2g), indicating that the Fe is in a partially oxidized state due to the partially carbonized Fe heterostructure. As shown in Figure S11, the pre-edge spectrum from Fe K-edge XANES has been further fitted into two peaks, which can be attributed to Fe and Fe_3C. The specific ratio between Fe_3C and Fe can be quantified by the corresponding peak areas.[45] Based on it, the ratio of Fe to Fe_3C is approximately 1.75:1, which is in high agreement with the XPS result (Figure 2e). As the Fourier transform extended X-ray absorption fine structure (FT-EXAFS) spectra of *R*-space shown in Figure 2h, there are two prominent peaks for $Fe_3C/Fe@PCNF-F$, which originate from the scattering paths of the Fe–C and Fe–Fe bonds, and demonstrate the formation of partially carbonized Fe_3C phase in the metallic Fe matrix.[46] The wavelet transform of c(*k*) (WT)-EXAFS with the maximum intensity at the (*k*, *R*) coordinate is closely associated with the atomic number (*Z*) and path length (*R*), which can provide pivotal clues for identifying the coordination environment. The $Fe_3C/Fe@PCNF-F$ shows two distinct scattering path signals at [χ (*k*), χ (*R*)] of about [7.8, 2.54] and [1.6, 1.95], which are related to the Fe–Fe and Fe–C paths, respectively (Figure 2i&S12). To determine the coordination parameters of $Fe_3C/Fe@PCNF-F$, we construct a reasonable structural model employing density functional theory (DFT) calculations on the basis of FT-EXAFS spectra and fitted data (Figure S13). The FT-EXAFS fitting data reveals that the Fe atoms in $Fe_3C/Fe@PCNF-F$ have two coordination roles corresponding to the Fe–C and Fe–Fe bonds. The FT-EXAFS fitting in *R*-space and *k*-space agrees with the experimental spectra of $Fe_3C/Fe@PCNF-F$ (Figure S14 and Table S1). The optimized lengths of Fe–Fe and Fe–C bonds in the Fe_3C/Fe model are in good agreement with the EXAFS fitted data, demonstrating the rationality of the Fe_3C/Fe model for the following DFT calculations. Furthermore, the pore structures of the $Fe_3C/Fe@PCNF$ and $Fe_3C/Fe@PCNF-F$ were investigated through the N_2 adsorption-desorption isotherms (Figure S15a). The distinct hysteresis loops suggest microporous and mesoporous structures coexist in $Fe_3C/Fe@PCNF$ and $Fe_3C/Fe@PCNF-F$. Based on the Brunauer–Emmett–Teller (BET) method, the specific surface areas of $Fe_3C/Fe@PCNF$ and $Fe_3C/Fe@PCNF-F$ are calculated to be 404.7 and 372.5 $m^2 g^{-1}$, respectively (Figure S15b). The micro-/mesoporous structure of $Fe_3C/Fe@PCNF-F$ originates from the decomposition of PVP molecules and zinc salt, resulting in a "molecular sieve" effect and preventing in situ generated aggregation of Fe_3C/Fe NPs. Consequently, the nitrogen reactants can penetrate into the PCNF and concentrate in its

cavities thermodynamically for the subsequent electrochemical N_2-fixation reactions near the surface of Fe_3C/Fe NPs.[47]

The interfacial environment related to the aerobic-hydrophobic Janus structure was assessed by a series of captive-bubble measurements. The N_2-bubble adhesion force on the $Fe_3C/Fe@CNF$, $Fe_3C/Fe@PCNF$, and $Fe_3C/Fe@PCNF-F$ catalysts was evaluated by touching their surfaces with N_2-bubbles in 0.1 M Na_2SO_4 electrolyte. As shown in Figure 3a–c, the $Fe_3C/Fe@PCNF$ and $Fe_3C/Fe@PCNF-F$ show aerophilic characters with stronger N_2 bubbles adhesive force when compared to that of $Fe_3C/Fe@CNF$. It can also be proven through the different deformations of the N_2 bubble (insets 1–3 of Figure 3a–c). The N_2 bubble contact angles on the $Fe_3C/Fe@CNF$, $Fe_3C/Fe@PCNF$, and $Fe_3C/Fe@PCNF-F$ surfaces reach to 151.6 ± 0.9°, 148.1 ± 1.3°, and 141.7 ± 0.5° (inset 4 of Figure 3a–c), respectively, demonstrating the most robust N_2 gas adhesion on the surface of the $Fe_3C/Fe@PCNF-F$ catalyst. It can be attributed to the continuous sorption of N_2 reactants into the $Fe_3C/Fe@PCNF-F$ catalyst that arises from the abundant nanoscopic cavities.[48,49] In addition, attributed to the protection provided by the pFDe layer (the concept proposed in Figure 1), the $Fe_3C/Fe@PCNF-F$ also possesses hydrophobic properties with a higher electrolyte contact angle of 153.1° (inset 5 of Figure 3c) than those of $Fe_3C/Fe@CNF$ (41.5°, inset 5 of Figure 3a) and $Fe_3C/Fe@PCNF$ (34.2°, inset 5 of Figure 3b). The advancing and receding contact angles of N_2 bubble and electrolyte contact angles for $Fe_3C/Fe@CNF$, $Fe_3C/Fe@PCNF$, and $Fe_3C/Fe@PCNF-F$ were fully summarized in Figure S16 and Table S2. The lowest advancing and receding contact angles of N_2 bubble further indicate the strong aerophilic property of the $Fe_3C/Fe@PCNF-F$. To demonstrate the advantages of the Janus structure in the $Fe_3C/Fe@PCNF-F$, *COMSOL* Multiphysics simulations were also conducted by constructing two models based on the experimental observation, where a hydrophobically modified layer of pFDe is wrapped around $Fe_3C/Fe@PCNF$ (Figure S17). By using the "transport of diluted species method", we can evaluate the two-phase (liquid and gas) concentration distributions during the diffusion process. The H_2O concentration drops sharply in the hydrophobic layer of $Fe_3C/Fe@PCNF-F$ as compared to the $Fe_3C/Fe@PCNF$ (Figure 3d–f), indicating the excellent H_2O resistibility of the as-covered fluorinated layer and as-induced limited H_2O around the electroactive Fe_3C/Fe NPs inside the $Fe_3C/Fe@PCNF-F$. On the contrary, sufficient N_2 gas can penetrate the interior of the $Fe_3C/Fe@PCNF-F$ with four times higher N_2 concentration in the center (site A) of $Fe_3C/Fe@PCNF-F$ than that of the $Fe_3C/Fe@PCNF$ counterpart (Figure 3g–i, Figure S18&19).

Furthermore, the electrochemical performance for nitrogen fixation reactions (NRR and NOR) was evaluated by using $Fe_3C/Fe@PCNF$ and $Fe_3C/Fe@PCNF-F$ catalysts in 0.1 M Na_2SO_4 electrolyte. To quantify the main product of NH_3 after the NRR process, the NH_3 yield rate was determined by averaging the values from the ultraviolet (UV) method and nuclear magnetic resonance (NMR) analysis with corresponding calibration curves shown in Figure S20. Before the electrochemical NRR tests, we
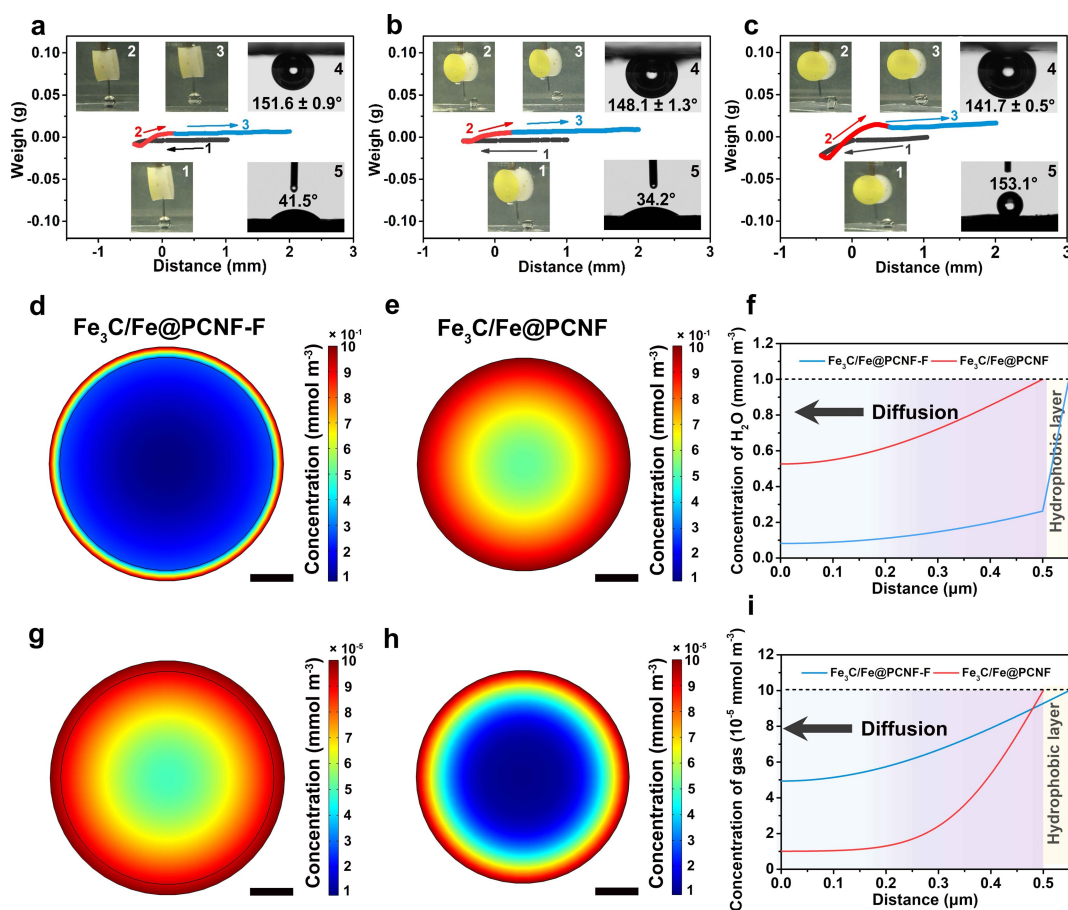
Figure 3. Characterization and *COMSOL* Multiphysics simulations of the aerobic-hydrophobic surface. a)–c) Nitrogen bubble adhesive force under 0.1 M Na$_2$SO$_4$ electrolyte and hydrophobic measurements of Fe$_3$C/Fe@CNF, Fe$_3$C/Fe@PCNF, and Fe$_3$C/Fe@PCNF-F catalysts. Insets 1–3 display the different N$_2$-bubble states during the adhesive force measurements. The insets 4–5 show the N$_2$-bubble contact angles under electrolyte and static-electrolyte-droplet contact angles. d)–f) The simulated distributions of H$_2$O concentration within 10^{-4} s for the Fe$_3$C/Fe@PCNF-F and Fe$_3$C/Fe@PCNF. g–i) The simulated distributions of N$_2$ gas concentration within 10^{-4} s for the Fe$_3$C/Fe@PCNF-F and Fe$_3$C/Fe@PCNF (scale-bar: 0.2 µm).

conducted a series of blank experiments to verify the purity of 0.1 M Na$_2$SO$_4$ electrolyte (Figure S21) and applied Ar/N$_2$ gases (Figure S22) without any detection of NH$_3$ contamination. Figure 4a shows the chronoamperometry curves for Fe$_3$C/Fe@PCNF-F over 2 h under different applied potentials from −0.1 to −0.5 V vs. reversible hydrogen electrode (RHE). Based on them, the normalized NH$_3$ yield rates and Faradaic efficiency (FE) values at each given potential were summarized in Figure 4b. In this regard, the Fe$_3$C/Fe@PCNF-F achieves a maximum NH$_3$ yield rate of 29.2 µg h^{-1} mg$^{-1}_{cat.}$ and an ultrahigh FE of 27.8 % at −0.2 V vs. RHE, which are higher than those of Fe$_3$C/Fe@PCNF (19.6 µg h^{-1} mg$^{-1}_{cat.}$, FE: 11.4 % at −0.2 V vs. RHE), and Fe$_3$C/Fe@CNF (10.6 µg h^{-1} mg$^{-1}_{cat.}$, FE: 6.5 % at −0.2 V vs. RHE). The excellent NRR performance of the as-prepared Fe$_3$C/Fe@PCNF-F was comparable with the NH$_3$ yields and FE values of the electrocatalysts reported previously (Table S3). The enhanced NRR performance of Fe$_3$C/Fe@PCNF-F can be attributed to the suppressed HER process with the existence of aerobic-hydrophobic layer, resulting in sufficient electrons supplied to reduce nitrogen

into ammonia molecules (Figure S23&S24). As the potential shifts negatively beyond −0.2 V vs. RHE, both the NH$_3$ yield rate and FE decrease significantly due to the competitive adsorption of hydrogen species on the electrocatalyst for the HER process. The Watt–Chrisp method (details in the Supporting Information) was conducted to exclude the by-product of N$_2$H$_4$ without detecting its signal (Figure S25&S26), demonstrating the excellent selectivity of Fe$_3$C/Fe@PCNF-F for NH$_3$ production. In order to eliminate any possible contaminants from the environment or electrocatalyst itself and to confirm the N source in produced NH$_3$, ^{15}N isotopic labeling experiments were further conducted qualitatively and quantitatively (Figure 4c&Figure S27). When the ^{15}N$_2$ gas is supplied as feeding gas, only two peaks indexed to ^{15}NH$_4^+$ can be observed in the NMR analysis, demonstrating that the detected ammonia originated from the supplied ^{15}N$_2$ completely rather than any NH$_3$ contaminants. After five consecutive cycles, the high NH$_3$ yield rate can be maintained without apparent fluctuation to prove the superior electrocatalytic NRR durability of Fe$_3$C/Fe@PCNF-F (Figure S28). The electrochemical NOR performance of
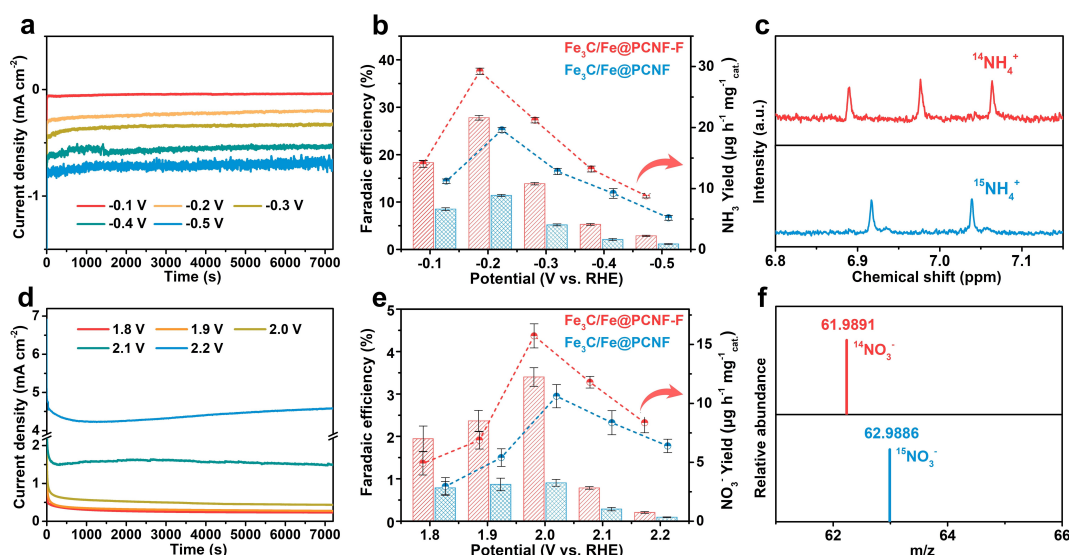
Figure 4. Electrochemical catalytic performance of NRR and NOR. a) Time dependence of current density for NRR with Fe$_3$C/Fe@PCNF-F catalyst at various applied potentials. b) NH$_3$ yield rate and Faradaic efficiency for NRR at various applied potentials. c) ^{1}H NMR analysis for NRR process fed by ^{14}N$_2$ and ^{15}N$_2$ gases with Fe$_3$C/Fe@PCNF-F catalyst. d) Time dependence of current density for NOR with Fe$_3$C/Fe@PCNF-F catalyst at various applied potentials. e) NO$_3^-$ yield rate and Faradaic efficiency for NOR at various applied potentials. f) MS spectra of both ^{14}NO$_3^-$ and ^{15}NO$_3^-$ from the NOR process fed by ^{14}N$_2$ and ^{15}N$_2$ gases (Fe$_3$C/Fe@PCNF-F is used as the catalyst).

Fe$_3$C/Fe@PCNF and Fe$_3$C/Fe@PCNF-F catalysts was systematically investigated in the same electrolytic cell. Figure 4d shows the chronoamperometry curves of Fe$_3$C/Fe@PCNF-F over 2 h at various applied potentials from 1.8 to 2.4 V vs. RHE, where the current density increases gradually with the increase of applied potential. The produced nitrate by the NOR process was estimated and quantified based on the standard methods by using UV method and high-performance ion chromatography (HPIC) in Figure S29. In particular, as shown in Figure 4e, the maximum nitrate yield rate and FE for Fe$_3$C/Fe@PCNF-F catalyst are achieved at a potential of 2.0 V vs. RHE to be 15.7 µg h^{-1} mg$^{-1}_{cat.}$ and 3.4%, respectively, which are much higher than those of Fe$_3$C/Fe@PCNF (10.6 µg h^{-1} mg$^{-1}_{cat.}$, FE: 0.9%), and Fe$_3$C/Fe@CNF (6.9 µg h^{-1} mg$^{-1}_{cat.}$, FE: 0.4%) with more comparisons in Table S4. To be noted, the Fe$_3$C/Fe@PCNF-F catalyst shows an attenuated OER process owing to the aerobic-hydrophobic Janus structure as confirmed by the linear-sweep voltammetry curves in Figure S30. Furthermore, we conducted time-dependent electrochemical NOR test to verify the continuous yield of nitrate product. The Fe$_3$C/Fe@PCNF-F shows a low-performance loss in the NO$_3^-$ harvest after five consecutive electrolysis cycles (Figure S31), proving its reasonable stability for the NOR process. Possible contaminations from the Fe$_3$C/Fe@PCNF-F catalyst and N$_2$ gas can also be ruled out as no NO$_3^-$ production was detected in N$_2$- and Ar-saturated electrolytes after 2 h test at open-circuit conditions (Figure S32). Furthermore, the ^{15}N isotope labeling experiments, as revealed by mass spectrometry (MS), were also performed in 0.1 M Na$_2$SO$_4$ electrolyte to trace the origin of nitrogen species in the NOR process (Figure 4f). The product solution obtained from the ^{15}N$_2$ saturated electrolyte

experiment exhibits a strong mass spectroscopy peak at *m/z* 62.9886 for ^{15}NO$_3^-$, compared with that of 61.9891 for ^{14}NO$_3^-$ in the ^{14}N$_2$ saturated electrolyte. The above results further indicate that the detected NO$_3^-$ is derived entirely from the electrochemical oxidation reaction of N$_2$. Meanwhile, it can be revealed that the partially carbonized iron heterojunction would be closely related to the enhanced nitrogen fixation performance (NH$_3$ and NO$_3^-$ yield rates; Faradaic efficiency values) when compared to the corresponding properties of Fe@PCNF-F and PCNF-F in Figure S33. Therefore, we have demonstrated that the pFDe modification on the porous carbon nanofibers is beneficial to constructing a robust "quasi-solid–gas" state microdomain around the catalyst surface for efficient and selective nitrogen fixation from both theoretical and experimental perspectives.

DFT calculations were also performed to investigate the structure–property relationship between the partially carbonized iron heterostructure and the enhanced performance for nitrogen fixation. The Fe$_3$C/Fe model has been constructed in Figure S13, based on the HR-TEM and EXAFS results. According to its calculated charge density distribution and corresponding two-dimensional slide (Figure 5a&b), it is found that an increased charge density area along the interface between Fe and Fe$_3$C phases is induced. The electrons of the Fe are prone to flow toward the adjacent Fe$_3$C phase via the heterogeneous interface, which results in the charge redistribution around the Fe–Fe$_3$C interface. This highly activated Fe$_3$C/Fe heterostructure would facilitate its coupling with N$_2$ molecules and accelerate the electron transfer to break the strong N≡N triple bonds (Figure 5c). To further unveil the possible reaction pathways on the partially carbonized iron heterojunction for
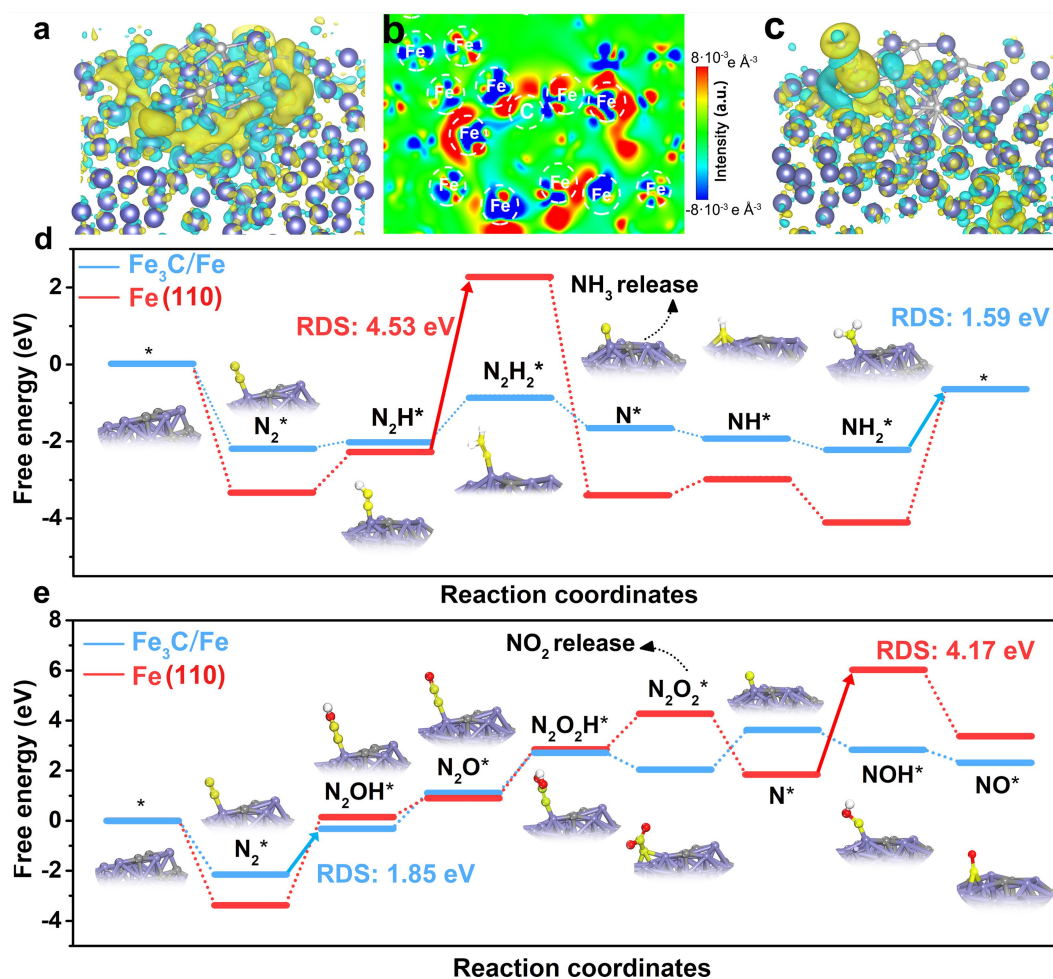
Figure 5. Reaction mechanism analysis of NRR and NOR based on DFT simulation results. a) The charge density difference of Fe₃C/Fe and b) corresponding 2D contour map section. c) The charge density difference of N_2 adsorption on Fe₃C/Fe (yellow area: electron accumulation; cyan area: electron depletion). d) Free-energy diagram for the NRR process with distal pathways on the Fe (110) and Fe₃C/Fe surfaces. e) Free-energy diagram for the NOR process on the Fe (110) and Fe₃C/Fe surfaces. The insets show the optimized Fe₃C/Fe structures with different intermediates during the electrocatalytic NRR and NOR processes. Color balls in the Figure: the violet, gray, dark blue, red, and while balls represent Fe, C, N, O, and H atoms, respectively.

nitrogen fixations (NRR and NOR), the Gibbs free energy (ΔG) profiles for each corresponding reaction intermediate are derived by DFT calculations. For the NRR process with an associative mechanism, the adsorbed N_2 molecules are initially hydrogenated to break the N≡N bond completely, resulting in the formation of NH_3 molecules simultaneously. The association pathway can even be divided into three types, including alternating pathway, distal pathway, and mixed pathway, based on different chemical steps in Figure S34. The conversion of N_2 to NH_3 on Fe₃C/Fe surface following the associative distal mechanism is energetically the most favorable pathway (geometries of the corresponding reaction intermediates are shown in Figure 5d). Regarding the distal pathway, the rate-determining step (RDS) on Fe₃C/Fe model is Step 7 ($NH_2^* \rightarrow ^*$) with a lower energy barrier of 1.59 eV. In the case of the alternating and mixed mechanisms on Fe₃C/Fe, the RDSs are both of Step 5 ($HN_2H_2^* \rightarrow H_2N_2H_2^*$ and $HN_2H_2^* \rightarrow NH^*$) with a higher energy barrier of 3.04 and 2.18 eV, respectively (Figure S35).

To demonstrate the structural advantage of the partially carbonized iron heterojunctions, we also constructed the Fe model as a comparison, where the Fe (110) surface is selected for nitrogen fixation. The high energy barriers of 4.53 and 1.77 eV on the Fe (110) and Fe₃C (121) surfaces indicate their negative role in reducing N_2 into NH_3, and demonstrate that the partially carbonized iron heterojunctions are beneficial to activating the Fe phase for boosted NRR performance (Figure S36). For the NOR process, the calculated relative energy pathways on both Fe₃C/Fe and Fe (110) models by DFT are shown in Figure 5e and Figure S37 in Supporting Information. To be specific, the N_2 molecule is absorbed on the catalyst surface and oxidized with the first OH⁻ to form N_2OH^* intermediate. The second OH⁻ will take H away to generate H_2O and N_2O^* intermediate. The last N–N bond breakage occurs at Step 6, where $N_2O_2^*$ evolves into N* intermediate and releases NO_2. The as-formed N* intermediate further continues to associate with OH⁻ and evolves to NO*. The NO* intermediate reacts
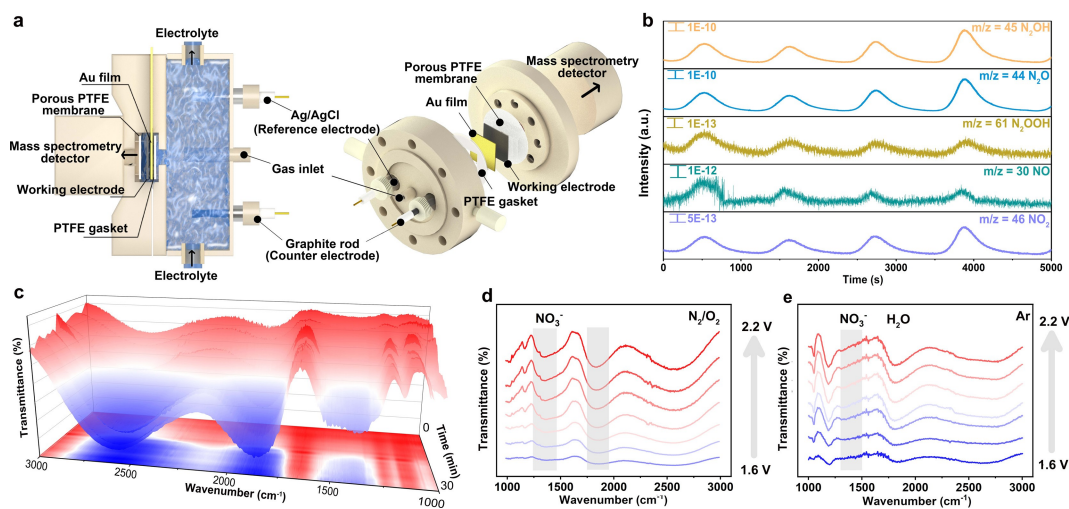
Figure 6. Operando spectroscopy for investigating the NOR mechanism experimentally. a) Schematic illustration of the operando DEMS. b) DEMS signals of gaseous intermediates/products during four times cycle. c) Three-dimensional operando FTIR spectra of $Fe_3C/Fe@PCNF-F$ at 2.0 V vs. RHE under different time. Operando FTIR spectra of $Fe_3C/Fe@PCNF-F$ under various potentials under d) N_2/O_2 and e) Ar atmospheres.

with O_2 and H_2O molecules to form NO_3^- via a non-electrochemical step (more detail in the Supporting Information).[50] Specifically, for the Fe (110) surface, the critical step is the formation of NOH* in Step 7 (N*→NOH*) with a high energy barrier of 4.17 eV. In contrast, the reduced energy barrier (1.85 eV) of RDS (Step 2, N_2*→N_2OH*) on the Fe_3C/Fe surface suggests that Fe_3C/Fe heterostructures can simultaneously achieve enhanced NOR performance. Therefore, it is rational that the partially carbonized iron phase in the Fe_3C/Fe heterostructure can activate the original Fe phase, and the optimized electronic structure achieves good coupling with N_2 molecules, which is responsible for promoting bifunctional nitrogen fixation.

These theoretical DFT results were further confirmed from an experimental perspective (taking the NOR process as an example), by conducting the differential electrochemical mass spectrometry (DEMS) and operando Fourier transform infrared (FTIR) spectroscopy in a customized electrochemical cell (Figure 6a). In the DEMS experiment, the catalyst was loaded on conductive carbon paper and connected electrically to the electrochemical workstation through a gold foil. The porous polytetrafluoroethylene (PTFE) membrane allows intermediates/products with different mass-to-charge ratios (*m*/*z*) to permeate and be detected at the mass spectrometry detector. The *m*/*z* signals of 45, 44, 61, 30, and 46 are detected periodically that correspond to N_2OH, N_2O, N_2OOH, NO, and NO_2 species, respectively (Figure 6b). Note that no signal is observed for the products of $N_2O_2H_2$ and HNO_2 species (Figure S38). This result favorably demonstrates that the NOR tends to proceed in the "end on" adsorption mode on the $Fe_3C/Fe@PCNF-F$, which matches well with the reaction mechanism based on the DFT calculations. To further verify the above mechanism, the time-resolved operando FTIR spectra of $Fe_3C/Fe@PCNF-F$ were collected at 2.0 V vs. RHE for 30 min (Figure 6c), where the vibration peak at about 1370 cm^{-1} for nitrate emerged and intensified gradually as

the time progressed. The operando FTIR spectra were collected during positive scans from 1.6 to 2.2 V vs. RHE (Figure 6d), where the vibration peak of nitrate at $\approx 1370 \text{ cm}^{-1}$ starts to appear since 1.8 V vs. RHE. No vibration peak of nitrate has been observed when carrying out the operando FTIR measurement under Ar atmosphere (Figure 6e), ruling out the possibility that the NO_3^- signals in Figure 6d originate from any other contaminants. Therefore, the reaction intermediates and products from NOR in $Fe_3C/Fe@PCNF-F$ are successfully detected by DEMS and operando FTIR, which is consistent with the results of our DFT calculations.

Conclusion

In summary, we report a selective and efficient bifunctional nitrogen fixation electrocatalyst by constructing an aerobic-hydrophobic Janus structure. It can be realized by introducing fluorinated modification on porous carbon nanofibers embedded with partially carbonized iron heterojunctions ($Fe_3C/Fe@PCNF-F$). Inspired by the unique structure of villus on abdomens of *Argyroneta aquatica*, the unique Janus structure can restrain water penetration into the interior of $Fe_3C/Fe@PCNF-F$ and endows a concentrated effect on N_2 molecules around the catalyst surface, resulting in the formation of a robust "quasi-solid–gas" state microdomain to suppress the competing reactions and overcome the mass-transfer limitations. Consequently, the $Fe_3C/Fe@PCNF-F$ exhibits excellent electrocatalytic performance for nitrogen fixation (NH_3 yield rate up to $29.2 \text{ μg h}^{-1} \text{ mg}^{-1}_{\text{cat.}}$ and Faraday efficiency (FE) up to 27.8% in NRR; NO_3^- yield rate up to $15.7 \text{ μg h}^{-1} \text{ mg}^{-1}_{\text{cat.}}$ and FE up to 3.4% in NOR). Density functional theory calculations elucidate the catalytic reaction mechanism on the Fe_3C/Fe heterostructure and reduce the energy barrier, which can also be verified from a variety of in situ characterizations to validate the

nitrogen fixation reaction pathway by the successful experimental detection of reaction intermediates. The aerobic-hydrophobic Janus structure provides new insight into designing efficient and selective electrocatalysts for nitrogen fixation.

Conflict of Interest

The authors declare no conflict of interest.

Data Availability Statement

The data that support the findings of this study are available from the corresponding author upon reasonable request.

Keywords: Aerobic-Hydrophobic · Bio-Inspired · Janus · Nitrogen Fixation · Quasi-Solid–Gas State

[1] M. A. Légaré, G. Blanger-Chabot, R. D. Dewhurst, E. Welz, I. Krummenacher, B. Engels, H. Braunschweig, *Science* **2018**, *359*, 896–900.

[2] B. H. R. Suryanto, H.-L. Du, D. Wang, J. Chen, A. N. Simonov, D. R. MacFarlane, *Nat. Catal.* **2019**, *2*, 290–296.

[3] B. M. Hoffman, D. Lukoyanov, Z. Y. Yang, D. R. Dean, L. C. Seefeldt, *Chem. Rev.* **2014**, *114*, 4041–4062.

[4] Y. Liu, M. Cheng, Z. He, B. Gu, C. Xiao, T. Zhou, Z. Guo, J. Liu, H. He, B. Ye, B. Pan, Y. Xie, *Angew. Chem. Int. Ed.* **2019**, *58*, 731–735.

[5] Y. Wang, Y. Yu, R. Jia, C. Zhang, B. Zhang, *Natl. Sci. Rev.* **2019**, *6*, 730–738.

[6] M. Cheng, C. Xiao, Y. Xie, *Adv. Mater.* **2021**, *33*, 2007891.

[7] Y. Wang, T. Li, Y. Yu, B. Zhang, *Angew. Chem. Int. Ed.* **2022**, *61*, e202115409.

[8] S. Li, J. Liang, P. Wei, Q. Liu, L. Xie, Y. Luo, X. Sun, *eScience* **2022**, *2*, 382–388.

[9] Y.-C. Hao, Y. Guo, L.-W. Chen, M. Shu, X.-Y. Wang, T.-A. Bu, W.-Y. Gao, N. Zhang, X. Su, X. Feng, J.-W. Zhou, B. Wang, C.-W. Hu, A.-X. Yin, R. Si, Y.-W. Zhang, C.-H. Yan, *Nat. Catal.* **2019**, *2*, 448–456.

[10] Y. T. Liu, X. Chen, J. Yu, B. Ding, *Angew. Chem. Int. Ed.* **2019**, *58*, 18903–18907.

[11] Z. Zhuang, L. Xia, J. Huang, P. Zhu, Y. Li, C. Ye, M. Xia, R. Yu, Z. Lang, J. Zhu, L. Zheng, Y. Wang, T. Zhai, Y. Zhao, S. Wei, L. Li, D. Wang, Y. Li, *Angew. Chem. Int. Ed.* **2023**, *62*, e202212335.

[12] L. Zhang, M. Cong, X. Ding, Y. Jin, F. Xu, Y. Wang, L. Chen, L. Zhang, *Angew. Chem. Int. Ed.* **2020**, *59*, 10888–10893.

[13] P. Xia, X. Pan, S. Jiang, J. Yu, B. He, P. M. Ismail, W. Bai, J. Yang, L. Yang, H. Zhang, M. Cheng, H. Li, Q. Zhang, C. Xiao, Y. Xie, *Adv. Mater.* **2022**, *34*, 2200563.

[14] H. He, H. Li, Q. Zhu, C. Li, Z. Zhang, M. Du, *Appl. Catal. B* **2022**, *316*, 121673.

[15] W. Li, Y. Ye, M. Jin, S. Zhang, C. Lin, C. Sun, Y. Zhang, G. Wang, C. Liang, H. Zhang, *Chem. Eng. J.* **2023**, *452*, 139494.

[16] G. J. Chao, L. S. Zhang, J. Tian, W. Fan, T. X. Liu, *Compos. Commun.* **2021**, *25*, 100703.

[17] X. Lin, L. Li, X. Chang, C. Pei, Z.-J. Zhao, J. Gong, *Sci. China Mater.* **2021**, *64*, 1173–1181.

[18] F. Lai, N. Chen, X. Ye, G. He, W. Zong, K. B. Holt, B. Pan, I. P. Parkin, T. Liu, R. Chen, *Adv. Funct. Mater.* **2020**, *30*, 1907376.

[19] F. Lai, J. Huang, X. Liao, W. Zong, L. Ge, F. Gan, Y. Fang, Y. Miao, J. Hofkens, T. Liu, L. Dai, *Adv. Mater.* **2022**, *34*, 2201853.

[20] H. Iriawan, S. Z. Andersen, X. Zhang, B. M. Comer, J. Barrio, P. Chen, A. J. Medford, I. E. L. Stephens, I. Chorkendorff, Y. Shao-Horn, *Nat. Rev. Methods Primers* **2021**, *1*, 56.

[21] A. Banerjee, B. D. Yuhas, E. A. Margulies, Y. Zhang, Y. Shim, M. R. Wasielewski, M. G. Kanatzidis, *J. Am. Chem. Soc.* **2015**, *137*, 2030–2034.

[22] Y. Chen, H. Liu, N. Ha, S. Licht, S. Gu, W. Li, *Nat. Catal.* **2020**, *3*, 1055–1061.

[23] Y. T. Liu, D. Li, J. Yu, B. Ding, *Angew. Chem. Int. Ed.* **2019**, *58*, 16439–16444.

[24] L. Tang, J. Dai, Y. Liu, Z. Li, T. Yi, L. Cai, J. Yu, B. Ding, *Compos. Commun.* **2021**, *23*, 100551.

[25] T. Zhang, W. Zong, Y. Ouyang, Y. Wu, Y. E. Miao, T. Liu, *Adv. Fiber Mater.* **2021**, *3*, 229–238.

[26] X. Yu, P. Hjuan, Z. Wei, L. Huang, Z. Gu, S. Peng, J. Ma, G. Zheng, *Joule* **2018**, *2*, 1610–1622.

[27] J. Zhu, L. Xia, R. Yu, R. Lu, J. Li, R. He, Y. Wu, W. Zhang, X. Hong, W. Chen, Y. Zhao, L. Zhou, L. Mai, Z. Wang, *J. Am. Chem. Soc.* **2022**, *144*, 15529–15538.

[28] W. Zong, H. Guo, Y. Ouyang, L. Mo, C. Zhou, G. Chao, J. Hofkens, Y. Xu, W. Wang, Y. E. Miao, Y.-E. Miao, G. He, I. P. Parkin, F. Lai, T. Liu, *Adv. Funct. Mater.* **2022**, *32*, 2110016.

[29] X. Liu, Y. Jiao, Y. Zheng, M. Jaroniec, S. Z. Qiao, *J. Am. Chem. Soc.* **2019**, *141*, 9664–9672.

[30] C. Tang, S. Z. Qiao, *Chem. Soc. Rev.* **2019**, *48*, 3166–3180.

[31] R. Battino, T. R. Rettich, T. Tominaga, *J. Phys. Chem. Ref. Data* **1984**, *13*, 563–600.

[32] J. Li, G. Chen, Y. Zhu, Z. Liang, A. Pei, C.-L. Wu, H. Wang, H. R. Lee, K. Liu, S. Chu, Y. Cui, *Nat. Catal.* **2018**, *1*, 592–600.

[33] S. S. Liu, T. Qian, M. F. Wang, H. Q. Ji, X. W. Shen, C. Wang, C. L. Yan, *Nat. Catal.* **2021**, *4*, 322–331.

[34] J. Zheng, Y. Lyu, M. Qiao, R. Wang, Y. Zhou, H. Li, C. Chen, Y. Li, H. Zhou, S. P. Jiang, S. Wang, *Chem* **2019**, *5*, 617–633.

[35] M. Tan, S. Tian, T. Zhang, K. Wang, L. Xiao, J. Liang, Q. Ma, G. Yang, N. Tsubaki, Y. Tan, *ACS Catal.* **2021**, *11*, 4633–4643.

[36] F. Lai, W. Zong, G. He, Y. Xu, H. Huang, B. Weng, D. Rao, J. A. Martens, J. Hofkens, I. P. Parkin, T. Liu, *Angew. Chem. Int. Ed.* **2020**, *59*, 13320–13327.

[37] A. Li, Q. Cao, G. Zhou, B. V. K. J. Schmidt, W. Zhu, X. Yuan, H. Huo, J. Gong, M. Antonietti, *Angew. Chem. Int. Ed.* **2019**, *58*, 14549–14555.

[38] M. Liu, S. Wang, L. Jiang, *Nat. Rev. Mater.* **2017**, *2*, 17036.

[39] D. Neumann, D. Woermann, *SpringerPlus* **2013**, *2*, 694.

[40] B. V. Hokmabad, S. Ghaemi, *Sci. Rep.* **2017**, *7*, 41448.

[41] Z. Tang, P. Wang, B. Xu, L. Meng, L. Jiang, H. Liu, *J. Am. Chem. Soc.* **2022**, *144*, 10950–10957.

[42] H. Guo, M. Zheng, X. Ma, R. Cao, K. Liu, W. Yang, S. Jian, S. Jiang, G. Duan, *Compos. Commun.* **2022**, *31*, 101130.

[43] X. Liang, J. Xiao, W. Weng, W. Xiao, *Angew. Chem. Int. Ed.* **2021**, *60*, 2120–2124.

[44] Y. Xing, Z. Yao, W. Li, W. Wu, X. Lu, J. Tian, Z. Li, H. Hu, M. Wu, *Angew. Chem. Int. Ed.* **2021**, *60*, 8889–8895.

[45] H. Simon, G. Cibin, I. Freestone, E. Schofield, *J. Phys. Condens. Matter* **2021**, *33*, 344002.

[46] W.-J. Jiang, L. Gu, L. Li, Y. Zhang, X. Zhang, L.-J. Zhang, J.-Q. Wang, J.-S. Hu, Z. Wei, L.-J. Wan, *J. Am. Chem. Soc.* **2016**, *138*, 3570–3578.

[47] T. Zhou, H. Shan, H. Yu, C. Zhong, J. Ge, N. Zhang, W. Chu, W. Yan, Q. Xu, H. Wu, C. Wu, Y. Xie, *Adv. Mater.* **2020**, *32*, 2003251.

[48] N. Han, K. R. Yang, Z. Lu, Y. Li, W. Xu, T. Gao, Z. Cai, Y. Zhang, V. S. Batista, W. Liu, X. Sun, *Nat. Commun.* **2018**, *9*, 924.

[49] X. Shan, J. Liu, H. Mu, Y. Xiao, B. Mei, W. Liu, G. Lin, Z. Jiang, L. Wen, L. Jiang, *Angew. Chem. Int. Ed.* **2020**, *59*, 1659–1665.

[50] M. Kuang, Y. Wang, W. Fang, H. T. Tan, M. X. Chen, J. D. Yao, C. T. Liu, J. W. Xu, K. Zhou, Q. Y. Yan, *Adv. Mater.* **2020**, *32*, 2002189.